SANDIA REPORT

SAND2019-5984
Unlimited Release
Printed May 2019

Kinetics of Failure in an Elastic Peridynamic Material

Stewart A. Silling

Prepared by
Sandia National Laboratories
Albuquerque, New Mexico 87185 and Livermore, California 94550

Sandia National Laboratories is a multimission laboratory managed and operated by National Technology & Engineering Solutions of Sandia LLC, a wholly owned subsidiary of Honeywell International Inc. for the U.S. Department of Energy National Nuclear Security Administration under contract DE-NA0003525.

Sandia National Laboratories

Issued by Sandia National Laboratories, operated for the United States Department of Energy by National Technology & Engineering Solutions of Sandia LLC.

Available to DOE and DOE contractors from
U.S. Department of Energy
Office of Scientific and Technical Information
P.O. Box 62
Oak Ridge, TN 37831

Telephone: (865) 576-8401
Facsimile: (865) 576-5728
E-Mail: reports@adonis.osti.gov
Online ordering: http://www.osti.gov/bridge

Available to the public from
U.S. Department of Commerce
National Technical Information Service
5285 Port Royal Rd
Springfield, VA 22161

Telephone: (800) 553-6847
Facsimile: (703) 605-6900
E-Mail: orders@ntis.fedworld.gov
Online ordering: http://www.ntis.gov/help/ordermethods.asp?loc=7-4-0#online

SAND2019-5984
Unlimited Release
Printed May 2019

Kinetics of Failure in an Elastic Peridynamic Material

Stewart A. Silling
Computational Multiscale Department
Sandia National Laboratories
P.O Box 5800
Albuquerque, NM 87185-1322

Abstract

The dynamic behavior of an elastic peridynamic material with a nonconvex bond potential is studied. In spite of the material's inherently unstable nature, initial value problems can be solved using essentially the same techniques as with conventional materials. In a suitably constructed material model, small perturbations grow exponentially over time until the material fails. The time for this growth is computed explicitly for a stretching bar that passes from the stable to the unstable phase of the material model. This time to failure represents an incubation time for the nucleation of a crack. The finiteness of the failure time in effect creates a rate dependence in the failure properties of the material. Thus, the unstable nature of the elastic material leads to a rate effect even though it does not contain any terms that explicitly include a strain rate dependence.

Acknowledgments

This work was performed under a Laboratory Directed Research and Development project at Sandia National Laboratories.

Contents

1 Introduction

This paper addresses the following question: Suppose the properties of an elastic material are such that under quasi-static loading, it fails when some critical strain is reached. When this strain is reached under loading at a finite rate, how much time does it take for the material to fail?

Material failure is observed in experiments to exhibit time- and rate-dependent phenomena. To account for these aspects of material failure, developers of failure models can include terms that depend explicitly on the rate of deformation or the speed of crack growth. For example, a dynamic fracture toughness can be assumed that depends on crack speed [13]. Alternatively, an incubation time can be applied in conjunction with the static fracture toughness [22, 3].

The present work seeks to derive time-dependent failure response from a model that does not include explicitly rate-dependent terms. Instead, the novel properties of peridynamic elastic materials with nonconvex micropotentials lead to time-dependent effects in the strain at which failure occurs. In this study, material failure emerges as the end result of the unstable growth of small disturbances in the nonconvex part of the micropotential, that is, the downward-sloping part of the curve of bond force vs. bond strain. In the peridynamic theory, these disturbances grow at a finite rate, or more precisely, their growth rate is of exponential order. This property permits solutions of initial value problems to be computed, both numerically and analytically, by conventional techniques.

The results in this paper include comparisons of analytically derived results with direct numerical simulations. The method used for these simulations is described in [25], which addresses the properties of the method with regard to accuracy and stability only for stable peridynamic materials. Jha and Lipton [8] analyze these properties in a similar numerical discretization method for nonconvex materials. They prove that the method is numerically stable and convergent, subject to certain restrictions. Additional papers by these authors also address finite element discretizations [7, 9].

The present paper is organized as follows. Section 2 contains a summary of the bond-based peridynamic equations. Section 3 discusses properties of nonconvex microelastic materials. In Section 4, the evolution of a small disturbance superposed on a finite displacement field is derived. A specific nonconvex material model is proposed in Section 5. Section 6 derives solutions for small sinusoidal perturbations in an unstable material. A similar problem with a Gaussian rather than sinusoidal perturbation is studied in Section 7. The time to failure of a bar undergoing stretch at a nominally uniform strain rate is discussed in Section 8. In Section 9, this time to failure is shown to imply a rate effect. Conclusions are given in Section 10.

2 Bond-based peridynamic theory

The peridynamic theory is a nonlocal theory of continuum mechanics [26] in which material points that are sufficiently close together interact directly with each other through a material model. The cutoff distance for interaction is called the *horizon*, denoted by δ, which can be finite or infinite. The equation of motion in one dimension has the form

$$\rho\ddot{u}(x,t) = \int_{-\delta}^{\delta} f(x+\xi, x)\, d\xi + b(x) \qquad \forall x,\ \forall t \tag{1}$$

where ρ, b, and u are the density, body force, and displacement respectively, and f is a *pairwise bond force density* function that specifies the force that the material point $x+\xi$ exerts on x. The vector ξ is called a *bond*. By convention, $\xi \neq 0$. The values of f are determined by the deformation according to the material model. To satisfy the balance of linear momentum, f is required to satisfy the condition

$$f(x+\xi, x) = -f(x, x+\xi) \qquad \forall x,\ \forall \xi. \tag{2}$$

In this paper, f is supplied by a *bond-based*, *nonlinear microelastic* material model, meaning that each pair of material points within each other's horizon interacts as though connected by a nonlinear spring:

$$f(x+\xi, x) = F(\eta, \xi), \qquad \eta = u(x+\xi) - u(x) \qquad \forall x,\ \forall \xi, \tag{3}$$

where F is a function such that

$$F(-\eta, -\xi) = -F(\eta, \xi) \qquad \forall \eta,\ \forall \xi. \tag{4}$$

The function w defined by

$$w(\eta, \xi) = \int_0^{\eta} F(z, \xi)\, dz \qquad \forall \eta,\ \forall \xi \tag{5}$$

is the *micropotential* for the microelastic material. It is related to the strain energy density W by

$$W(x) = \frac{1}{2}\int_{-\delta}^{\delta} w(\eta, \xi)\, d\xi \qquad \forall x. \tag{6}$$

If

$$w_{\eta\eta}(\eta, \xi) > 0 \qquad \forall \eta,\ \forall \xi \tag{7}$$

then the microelastic material is *convex*. Otherwise, it is *nonconvex*. The materials studied in this paper are nonconvex, because they possess both an upward sloping and a downward sloping segment of the curve of F vs. η.

Of interest in this paper are motions in which a small incremental displacement field $\tilde{u}$ is superposed on a time-independent, homogeneous deformation with strain ϵ_0:

$$u(x,t) = \epsilon_0 x + \tilde{u}(x,t) \qquad \forall x,\ \forall t. \tag{8}$$

Assume $b \equiv 0$ throughout the region. From (3) and (8), we adopt the following linear approximation to the material model:

$$F(\epsilon_0\xi + \tilde{\eta}, \xi) = F(\epsilon_0\xi, \xi) + \tilde{F}(\tilde{\eta}, \xi), \qquad \tilde{\eta} = \tilde{u}(x+\xi) - \tilde{u}(x) \tag{9}$$

where the incremental bond force density $\tilde{F}$ is given by

$$\tilde{F}(\tilde{\eta}, \xi) = C(\xi)\tilde{\eta}, \qquad C(\xi) = \frac{\partial F}{\partial \eta}(\epsilon_0\xi, \xi) \qquad \forall \tilde{\eta},\ \forall \xi. \tag{10}$$

C is called the *micromodulus* function. By (4) and (10), C has the following symmetry:

$$C(-\xi) = C(\xi) \qquad \forall \xi. \tag{11}$$

Since the homogeneous deformation by itself is in equilibrium, and since by assumption $\tilde{u}$ is small, the equation of motion (1) with the linearized material model (10) becomes

$$\rho \ddot{\tilde{u}}(x,t) = \int_{-\delta}^{\delta} C(\xi)(\tilde{u}(x+\xi) - \tilde{u}(x))\, d\xi \qquad \forall x,\ \forall t \tag{12}$$

which is formally the same as in Kunin's nonlocal theory, but with a cutoff distance for interactions [14]. More details about the linearized bond-based peridynamic equations can be found in [24].

3 Nonconvex micropotentials

The usual assumption about C is that it is non-negative for all ξ, since this property implies material stability. However, of particular interest in this paper are materials in which C can be negative, as shown in Figure 1.

Lipton [15, 16] studied the properties of microelastic peridynamic materials of this type, which are obtainable from a nonconvex micropotential. He proved that in spite of their inherent instability, initial value problems with these materials can be well-posed. Moreover, a suitably parameterized class of such material models, in which the critical energy release rate is independent of horizon, has remarkable convergence properties in the limit of zero horizon. Under appropriate conditions, this limit recovers a Griffith crack with the same prescribed critical energy release rate, while material points off of the crack set obey the local equations of solid mechanics. The practical nature of nonconvex peridynamic materials in simulating complex phenomena in dynamic fracture is demonstrated by Lipton, Lehoucq, and Jha [17]. Further analysis and demonstration of these features is given by Lipton, Said, and Jha [19, 18],

Nonconvex peridynamic material models can also reproduce features of deformation-induced phase transformations. Dayal and Bhattacharya [4] studied a class of such microelastic materials in which two stable (upward sloping) branches of the bond force vs. bond strain curve are separated by an unstable (downward sloping) branch. Numerical solutions under suitable boundary conditions show that the body segregates itself in equilibrium into two stable phases. The phase boundary between the phases has a finite thickness and a complex structure in which *some* bonds necessarily occupy the unstable branch. These results demonstrate that a stable equilibrium deformation can contain bonds in the unstable part of the material model. This behavior is consistent with the results of Mengesha and Du [20]. Aguiar, Royer-Carfagni, and Seitenfuss [1] analyzed a nonconvex peridynamic material with two stable branches that produces equilibrium deformations with a repeating pattern of localizations. These localizations are strongly affected by the way boundary conditions are applied in a bar of finite length.

The possibility of having stable deformations containing some unstable bonds is in contrast to the local theory, in which Hadamard instability (loss of strong ellipticity) cannot occur in a stable equilibrium deformation within a finite volume. Nevertheless, loss of strong ellipticity in the local theory is a necessary condition for the onset of interesting phenomena such as phase changes [5, 10, 11, 12, 6, 27]. Loss of ellipticity is sometimes used as a criterion to nucleate or grow a crack or other localization in enriched finite element techniques [2].

In an unbounded peridynamic body using the linearized model, plane waves can be studied by assuming the following displacement field:

$$u(x,t) = Ae^{i(kx-\omega t)} \qquad \forall x,\ \forall t \tag{13}$$

where A is the amplitude, k is the wavenumber, and ω is the angular frequency, which in general depends on the wavenumber. The quantities k and ω are related to the wavelength Λ and the frequency ν by the elementary relations

$$k = \frac{2\pi}{\Lambda}, \qquad \omega = \frac{2\pi}{\nu}. \tag{14}$$

To derive the relation between k and ω, combine (12) (omitting the superscript from $\tilde{u}$) and (13) to yield

$$\begin{aligned}
\rho\omega^2 &= \int_{-\delta}^{\delta} C(\xi)\left(1 - e^{ik\xi}\right)\, d\xi \\
&= \int_{-\delta}^{\delta} C(\xi)\left(1 - \cos k\xi\right)\, d\xi \\
&= P - \int_{-\delta}^{\delta} C(\xi)\cos k\xi\, d\xi \\
&= P - \bar{C}(k) \qquad \forall k
\end{aligned} \tag{15}$$

where $\bar{C}$ and P are defined by

$$\bar{C}(k) = \int_{-\delta}^{\delta} C(\xi) \cos k\xi \, d\xi, \qquad P = \bar{C}(0) = \int_{-\delta}^{\delta} C(\xi) \, d\xi. \tag{16}$$

Observe that $\bar{C}$ is the Fourier transform of C:

$$\bar{C}(k) = \int_{-\delta}^{\delta} C(\xi) e^{-ik\xi} \, d\xi \qquad \forall k. \tag{17}$$

For typical engineering analysis, one deals with materials for which ω^2 as determined by (15) is non-negative, as illustrated by the blue curve in the right hand plot in Figure 2. In this case, the wave phase velocity given by

$$\mathcal{V}(k) = \pm \frac{\omega(k)}{k} \qquad \forall k \tag{18}$$

is real, with the $+$ and $-$ signs corresponding to waves moving in the $+x$ or $-x$ directions respectively. However, of primary interest in the remainder of this paper are choices of the micromodulus function $C(\xi)$ such that the curve of $\omega^2(k)$ is non-positive; hence, formally, $\omega(k)$ and $\mathcal{V}(k)$ are imaginary.

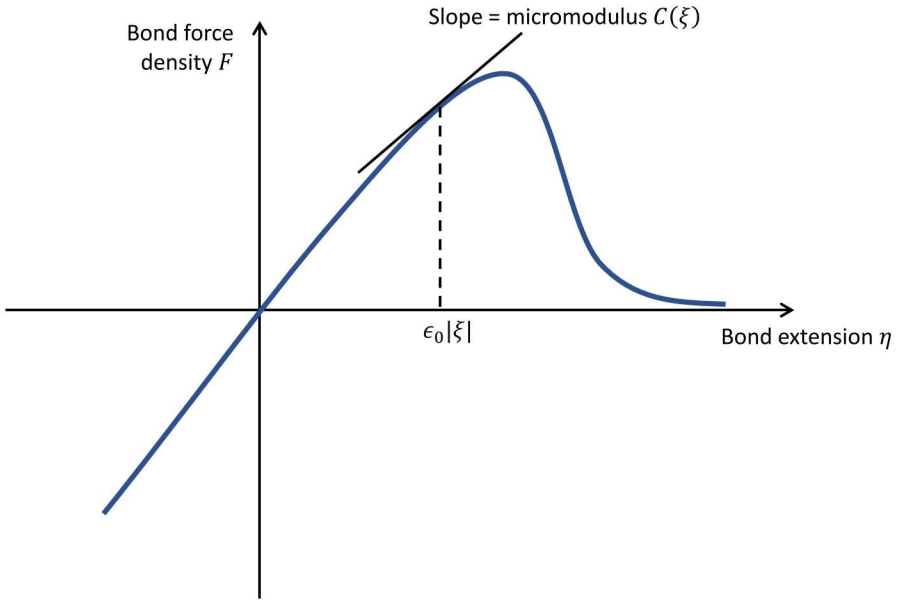

Figure 1. Nonlinear material model for bond force density. The bond vector is ξ.

4 Stable waves and unstable waveforms

Suppose, in an infinite, homogeneous peridynamic bar, an initial condition is given by

$$u(x,0) = A\cos kx, \qquad \dot{u}(x,0) = 0 \qquad \forall x \tag{19}$$

where k is a given wavenumber. If $\omega^2(k) >= 0$ as determined by (15), then D'Alembert's solution yields

$$u(x,t) = \frac{A}{2}\left[\cos(kx - \omega(k)t) + \cos(kx + \omega(k)t)\right] \qquad \forall x,\ \forall t. \tag{20}$$

If, on the other hand, $\omega^2(k) < 0$, then the displacement field is given by

$$u(x,t) = A\cos(kx)\cosh(\lambda(k)t) \qquad \forall x,\ \forall t \tag{21}$$

where

$$\lambda(k) = \sqrt{-\omega^2(k)} > 0 \qquad \forall k. \tag{22}$$

An important feature of the displacement field in (21) is that unlike the stable solution (20), the wave does not propagate; it stays in the same place while it grows. The local strain in such an unstable waveform is found from

$$\epsilon(x,t) = u_x(x,t) = -Ak\sin(kx)\cosh(\lambda(k)t) \qquad \forall x,\ \forall t. \tag{23}$$

For large times, since $\cosh z := (e^z + e^{-z})/2$, the decaying exponential terms in (21) and (23) become negligible, yielding

$$\epsilon(x,t) \sim -\frac{Ak}{2}e^{\lambda(k)t}\sin(kx) \qquad \forall x,\ t \to \infty. \tag{24}$$

The function $\lambda(k)$ is called the *blow-up rate* for wavenumber k. In general, $\lambda(k)$ is bounded except for materials in which $C(\xi)$ is singular at $\xi = 0$. Another feature of unstable peridynamic materials is that $\lambda(0) = 0$, implying that very long wavelengths grow very slowly over time. It will be shown below that the high-wavenumber limit of $\lambda(k)$ dominates the type of instability that occurs in modeling crack nucleation.

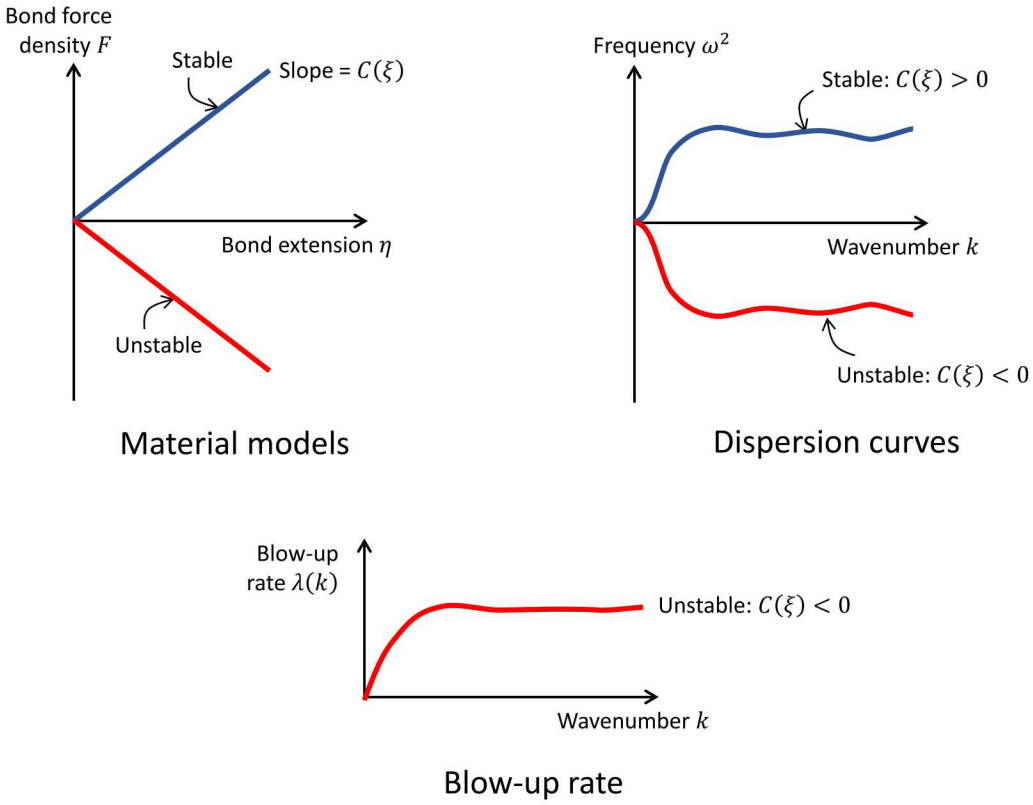

Figure 2. Stable and unstable peridynamic materials and their dispersion curves.

5 Example of a nonconvex material model

Let s denote the *bond strain* defined by

$$s(\eta,\xi) = \frac{\eta}{\xi} \qquad \forall \eta,\ \forall \xi. \tag{25}$$

(Recall that $\xi \neq 0$.) Consider the nonlinear material whose bond force density is given by

$$F(\eta,\xi) = \frac{\xi}{\delta} \begin{cases} cs & \text{if } s < s_1, \\ cs_1(s_0 - s)/(s_0 - s_1) & \text{if } s_1 \leq s < s_0, \\ 0 & \text{if } s_0 \leq s \end{cases} \tag{26}$$

$\forall \eta,\ \forall \xi$, where c, s_1, and s_0 are positive constants, $s_1 < s_0$. This material model is illustrated in Figure 3.

It is helpful to compute the Young's modulus E for the material model (26) for a given value of c. To do this, subject a bar to a constant small strain ϵ, where $\epsilon < s_1$. Using (26), the stress $\sigma = E\epsilon$ at any point in the bar, say $x = 0$, is computed by summing the forces in all the peridynamic bonds that cross this point:

$$\begin{aligned} E\epsilon &= \int_0^\delta \xi F(\epsilon\xi, \xi)\, d\xi \\ &= \int_0^\delta \xi \left(\frac{c\epsilon\xi}{\delta}\right)\, d\xi \\ &= \frac{c\epsilon\delta^2}{3} \end{aligned} \tag{27}$$

hence

$$c = \frac{3E}{\delta^2}. \tag{28}$$

The corresponding speed of small amplitude, long wavelength elastic waves is therefore given by

$$\mathcal{C} = \mathcal{V}(0) = \sqrt{\frac{E}{\rho}} = \sqrt{\frac{c\delta^2}{3\rho}}. \tag{29}$$

Let an infinite bar be composed of the material (26). Consider an incremental displacement field superposed on a homogeneous deformation as in (8):

$$u(x,t) = \epsilon_0 x + \tilde{u}(x,t) \qquad \forall x,\ \forall t. \tag{30}$$

Suppose further that

$$s_1 < \epsilon_0 < s_0. \tag{31}$$

Therefore, the bar is in the unstable branch of the material model (26) for all bonds ξ. The linearized material model for the subsequent evolution of the bar is given by

$$\tilde{F}(\tilde{\eta},\xi) = -C'(\xi)\tilde{\eta} \qquad \forall \tilde{\eta},\ \forall \xi, \qquad C'(\xi) = \frac{cs_1}{(s_0 - s_1)\delta} > 0. \tag{32}$$

From (15) and (32), the frequency of a wave with wavenumber k is found from

$$\begin{aligned} \rho\omega^2(k) &= -\int_{-\delta}^{\delta} C'(\xi)\,(1 - \cos k\xi)\ d\xi \\ &= \frac{-2cs_1}{(s_0 - s_1)\delta} \int_0^\delta (1 - \cos k\xi)\, d\xi \\ &= \frac{-2cs_1}{s_0 - s_1} \int_0^1 (1 - \cos(k\delta p))\, dp \\ &= \frac{-2cs_1}{s_0 - s_1} \left[1 - \frac{\sin k\delta}{k\delta}\right] \qquad \forall k \end{aligned} \tag{33}$$

where $p = \xi/\delta$. From (22) and (33), the blow-up rate for wavenumber k is given by

$$\lambda(k) = \sqrt{\frac{2cs_1}{(s_0 - s_1)\rho}\left[1 - \frac{\sin k\delta}{k\delta}\right]} \qquad \forall k. \tag{34}$$

A graph of this curve is shown on the left in Figure 4. From (29) and (34), an alternate form of (34) is given by

$$\lambda(k) = \frac{\mathcal{C}}{\delta}\sqrt{\frac{6s_1}{(s_0 - s_1)}\left[1 - \frac{\sin k\delta}{k\delta}\right]} \qquad \forall k. \tag{35}$$

Figure 4 also shows the blow-up rate as a function of wavenumber that occurs in the local theory for a similar unstable material. The main feature is that the local curve increases unboundedly, while the nonlocal curve from (34) is bounded. This difference results in dramatically different results in solving initial value problems as shown on the right in Figure 4. This plot shows the strain field that is predicted numerically for the local and nonlocal models for an infinite bar in the unstable part of the material model with a small initial sinusoidal perturbation. As will be shown in detail in Section 6, the nonlocal strain field grows over time, but this growth is of exponential order. In contrast, the local solution is not of exponential order and is therefore "more unstable" than the nonlocal solution. The highly chaotic and intractable nature of unstable elastic materials in the local theory is the reason that the analysis in the remainder of this paper is possible within peridynamics but not in the local theory.

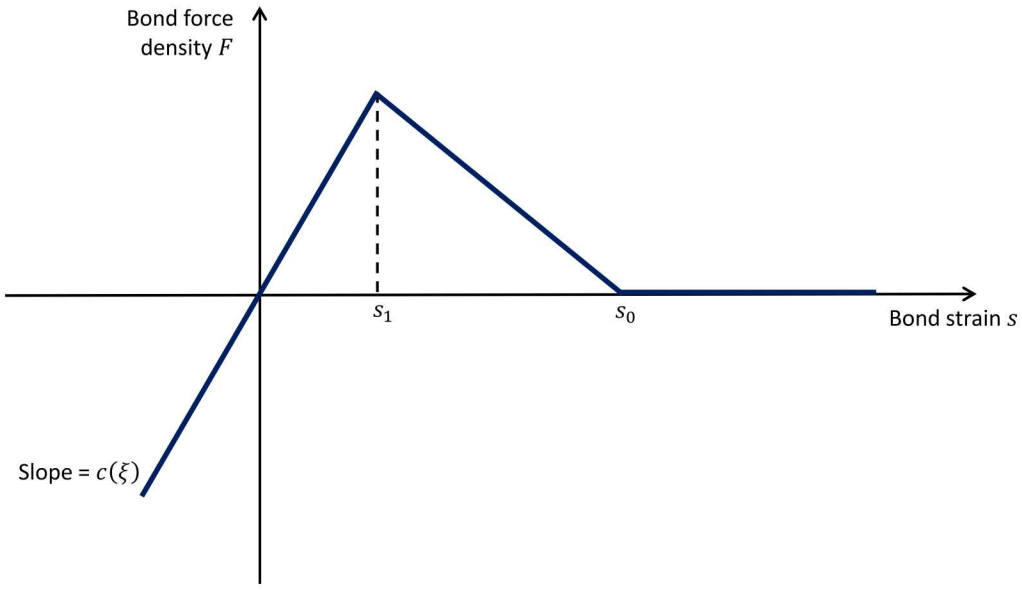

Figure 3. Material model in equation (26).

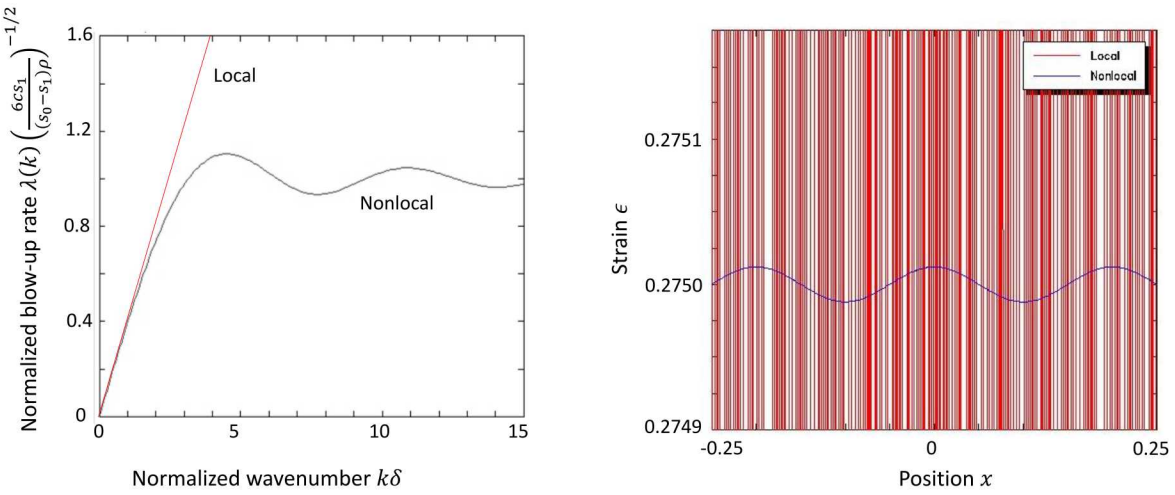

Figure 4. Left: Blow-up rate as a function of wavenumber for the material in the unstable part of (26). Right: Numerical simulations of strain in a bar starting from a small sinusoidal perturbation demonstrate that the nonlocal model gives more sensible results than the PDE theory for unstable elastic materials.

6 Unstable growth of a small sinusoidal perturbation

Consider a homogeneous bar composed of the material (26). Let Λ be a constant wavelength. Suppose the bar has initial conditions given by

$$u(x,0) = \epsilon_0 x + \frac{\tilde{\epsilon}_0}{k}\sin(kx), \qquad \dot{u}(x,0) = 0 \qquad \forall x \tag{36}$$

where $\tilde{\epsilon}_0$ is a small constant and

$$\epsilon_0 = \frac{s_1 + s_0}{2}, \qquad k = \frac{2\pi}{\Lambda}. \tag{37}$$

These initial conditions consist of a small oscillatory perturbation with strain amplitude $\tilde{\epsilon}_0$ superposed on a homogeneous deformation. The homogeneous deformation has a strain that is centered in the downward sloping segment of the material model shown in Figure 3.

For this initial value problem, let t_{fail} denote the time at which the local strain first exceeds s_0 at some point in the bar. From (23) and (36), this condition is found from

$$\epsilon_0 + \tilde{\epsilon}_0 \cosh(\lambda(k) t_{fail}) = s_0, \tag{38}$$

thus

$$t_{fail} = \frac{1}{\lambda(k)} \cosh^{-1}\left(\frac{s_0 - \epsilon_0}{\tilde{\epsilon}_0}\right). \tag{39}$$

Figure 5 shows the evolution of the strain field for a sequence of times at a constant time interval of $\Delta t = 0.096$. The material model parameters are $\delta = 0.1$, $E = 1$, $\rho = 1$, $s_1 = 0.05$, $s_0 = 0.20$. The amplitude of the initial strain perturbation is $\tilde{\epsilon}_0 = 1.0 \times 10^{-6}$. The wavelength of the perturbation is $\Lambda = 3\delta$.

Figure 6 shows the strain at the point $x = 0$ as a function of time for three values of wavelength of the initial perturbation: $\Lambda = \delta/5$, 3δ, and 5δ. Both the numerical solution and the analytical estimate (24) are shown for each value of Λ. There are two key features of these results. First, there is a substantial period of time that passes before the solutions visibly blow up. Second, the rate of the blow-up is dependent on the wavelength of the initial data, as shown schematically in the lower graph in Figure 2.

Figure 7 is a graph of the failure time t_{fail} as a function of the wavelength of the initial perturbation Λ. The failure times from the analytic expression (39) and direct numerical simulation are shown, which agree closely.

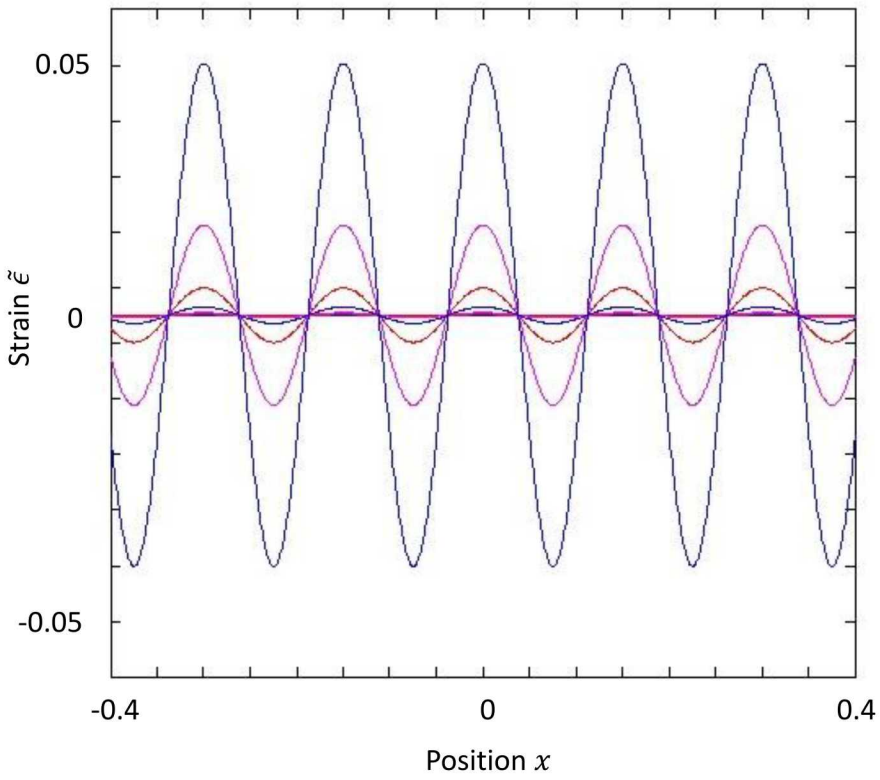

Figure 5. Strain field at a sequence of times for unstable growth of a small sinusoidal perturbation.

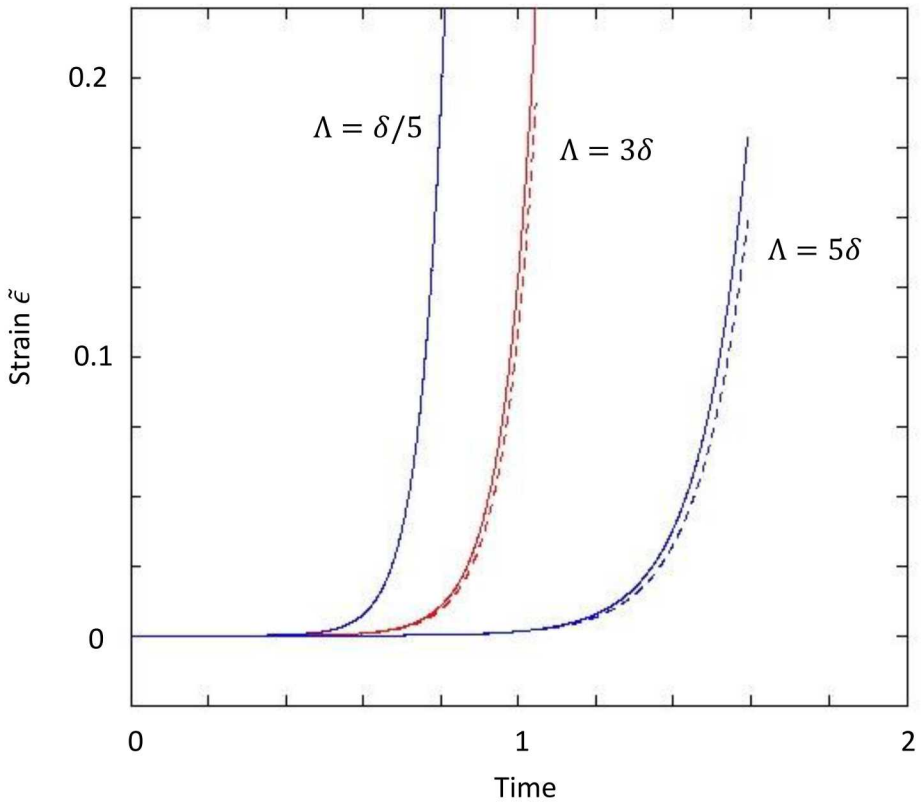

Figure 6. Growth over time of the strain at the point $x = 0$ for unstable growth of a small sinusoidal perturbation. Solid lines are the numerical solution; dashed lines are from the estimate (24).

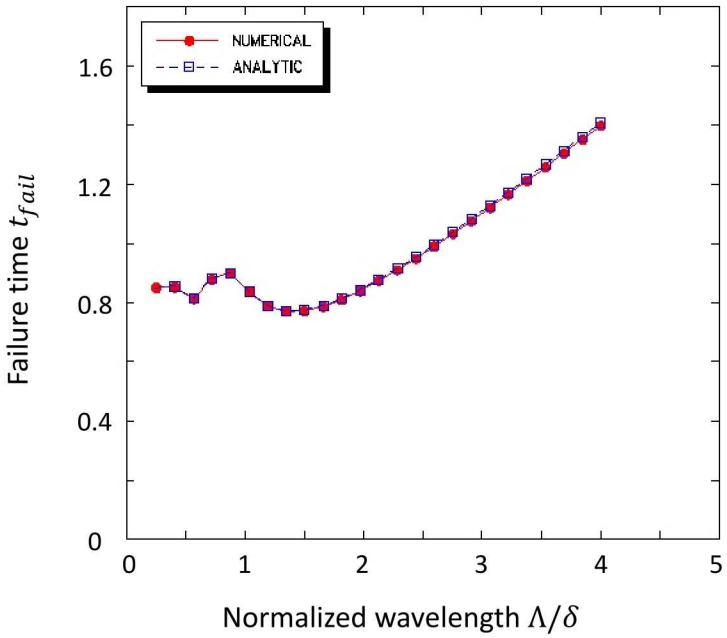

Figure 7. Failure times for growth of an initial sinusoidal perturbation whose strain amplitude is 1.0×10^{-6}. The solid blue line is from the direct numerical simulation; the red dashed line is from the analytical expression (39).

7 Failure nucleated at a Gaussian perturbation

A slight modification of the initial conditions in Section 6 gives insight into the process of crack nucleation. Instead of (36), let the bar have initial conditions given by

$$u(x,0) = \epsilon_0 x + \tilde{u}_0(x), \qquad \dot{u}(x,0) = 0 \qquad \forall x \tag{40}$$

where

$$\tilde{u}_0(x) = \frac{\sqrt{\pi}\ell\tilde{\epsilon}_0}{2}\mathrm{erf}(x/\ell) \qquad \forall x \tag{41}$$

and where $\tilde{\epsilon}_0$ is a small constant, ℓ is a constant length scale, erf is the error function defined by

$$\mathrm{erf}(z) = \frac{2}{\sqrt{\pi}}\int_0^z e^{-y^2}\, dy \qquad \forall z, \tag{42}$$

and ϵ_0 is such that

$$s_1 + \tilde{\epsilon}_0 < \epsilon_0 < s_0 - \tilde{\epsilon}_0. \tag{43}$$

The initial local strain is found from (40), (41), and (42) to be given by

$$u_x(x,0) = \epsilon_0 + \tilde{u}_{0x}(x), \qquad \tilde{u}_{0x}(x) = \tilde{\epsilon}_0 e^{-(x/\ell)^2} \qquad \forall x. \tag{44}$$

Unlike the sinusoidal perturbation considered in the previous Section, the present initial conditions include a spectrum of Fourier components. To find the solution, the Fourier transform and its inverse will be used. For any function $v(x)$, let

$$\bar{v}(k) = \mathcal{F}\{v\}(k) = \int_{-\infty}^{\infty} e^{-ikx} v(x)\, dx \qquad \forall k, \tag{45}$$

$$v(x) = \mathcal{F}^{-1}\{\bar{v}\}(x) = \frac{1}{2\pi}\int_{-\infty}^{\infty} e^{ikx}\bar{v}(k)\, dk \qquad \forall x. \tag{46}$$

The transform of the Gaussian function with half-width ℓ is given by the standard identity

$$\mathcal{F}\{e^{-(x/\ell)^2}\}(k) = \sqrt{\pi}\ell e^{-(\ell k/2)^2} \qquad \forall k. \tag{47}$$

Linearizing the equation of motion (12) near the homogeneous field $u = \epsilon_0 x$ leads to

$$\rho\ddot{\tilde{u}}(x,t) = -\int_{-\delta}^{\delta} C'(\xi)(\tilde{u}(x+\xi) - \tilde{u}(x))\, d\xi \qquad \forall x,\ \forall t \tag{48}$$

where $C'(\xi)$ is positive and is given by (32). Differentiating (48) with respect to x gives a relation for the local strain field,

$$\rho\ddot{\tilde{u}}_x(x,t) = -\int_{-\delta}^{\delta} C'(\xi)(\tilde{u}_x(x+\xi) - \tilde{u}_x(x))\, d\xi \qquad \forall x,\ \forall t. \tag{49}$$

Taking the transform of (49) using (45) results in

$$\rho\ddot{\bar{\tilde{u}}}_x(k,t) = (P' - \bar{C}'(k))\bar{\tilde{u}}_x(k,t), \qquad \forall k,\ \forall t \tag{50}$$

where

$$P' = \int_{-\delta}^{\delta} C'(\xi)\, d\xi = \bar{C}'(0). \tag{51}$$

The solution to the ordinary differential equation (50) with initial conditions (40) is given by

$$\bar{\tilde{u}}_x(k,t) = \bar{\tilde{u}}_{0x}(k,t)\cosh(\lambda(k)t) \qquad \forall k,\ \forall t \tag{52}$$

where

$$\lambda(k) = \sqrt{\frac{P' - \bar{C}'(k)}{\rho}} \qquad \forall k. \tag{53}$$

From (44), (47), and (52),

$$\bar{\tilde{u}}_x(k,t) = \sqrt{\pi}\ell\tilde{\epsilon}_0 e^{-(\ell k/2)^2}\cosh(\lambda(k)t) \qquad \forall k,\ \forall t. \tag{54}$$

Applying the inverse transform (46) to (54) yields

$$\tilde{u}_x(x,t) = \frac{\ell\tilde{\epsilon}_0}{2\sqrt{\pi}}\int_{-\infty}^{\infty} e^{ikx-(\ell k/2)^2}\cosh(\lambda(k)t)\ dk \qquad \forall x,\ \forall t. \tag{55}$$

Since the peak initial strain occurs at $x = 0$, it is reasonable to assume that failure eventually occurs first at this point. From (55),

$$\tilde{u}_x(0,t) = \frac{\ell\tilde{\epsilon}_0}{2\sqrt{\pi}}\int_{-\infty}^{\infty} e^{-(\ell k/2)^2}\cosh(\lambda(k)t)\ dk \qquad \forall t. \tag{56}$$

If the initial displacement perturbation occurs over a small distance, that is, if $\ell < \delta$, then the Gaussian term in the integrand in (56) spreads out over a large range of k. As illustrated in Figure 4, for large k, the curve of $\lambda(k)$ approaches a plateau:

$$\lambda(k) \to \lambda_\infty := \sqrt{P'/\rho} \quad \text{as} \quad k \to \infty. \tag{57}$$

Under this assumption of small ℓ, therefore,

$$\begin{aligned}
\tilde{u}_x(0,t) &\approx \frac{\ell\tilde{\epsilon}_0}{2\sqrt{\pi}}\cosh(\lambda_\infty t)\int_{-\infty}^{\infty} e^{-(\ell k/2)^2}\ dk \\
&= \frac{\ell\tilde{\epsilon}_0}{2\sqrt{\pi}}\cosh(\lambda_\infty t)\left(\frac{2\sqrt{\pi}}{\ell}\right) \\
&= \tilde{\epsilon}_0\cosh(\lambda_\infty t) \qquad \forall t.
\end{aligned} \tag{58}$$

The material property P' is related to the *stability index* Z defined [23, 17] by

$$P' = -Z, \qquad \lambda_\infty = \sqrt{\frac{-Z}{\rho}}.$$

The condition $Z < 0$ is a criterion for the growth of a discontinuous perturbation in the displacement field. The limit $\ell \to 0$ in the above analysis represents, in effect, such a jump discontinuity. It is therefore not surprising that Z enters into the limiting result (58). The "crack nucleation criterion" $Z < 0$ is a specialization to the 1D homogeneous case of a more general result in multiple dimensions in which Z is essentially the smallest eigenvalue of the acoustic tensor for small wavelengths.

As in Section 6, the time to failure t_{fail} is defined to be the time required for the peak local strain to exceed s_0. Therefore (56) leads to

$$s_0 - \epsilon_0 = \frac{\ell\tilde{\epsilon}_0}{2\sqrt{\pi}}\int_{-\infty}^{\infty} e^{-(\ell k/2)^2}\cosh(\lambda(k)t_{fail})\ dk. \tag{59}$$

Using (58), the assumption of small ℓ allows t_{fail} to be computed in closed form:

$$t_{fail} \approx \frac{1}{\lambda_\infty}\cosh^{-1}\left(\frac{s_0 - \epsilon_0}{\tilde{\epsilon}_0}\right). \tag{60}$$

The blow-up rate λ_∞ can be expressed in terms of more basic quantities by evaluating (35) with $k \to \infty$:

$$\lambda_\infty = \frac{\mathcal{C}}{\delta}\sqrt{\frac{6s_1}{s_0 - s_1}}. \tag{61}$$

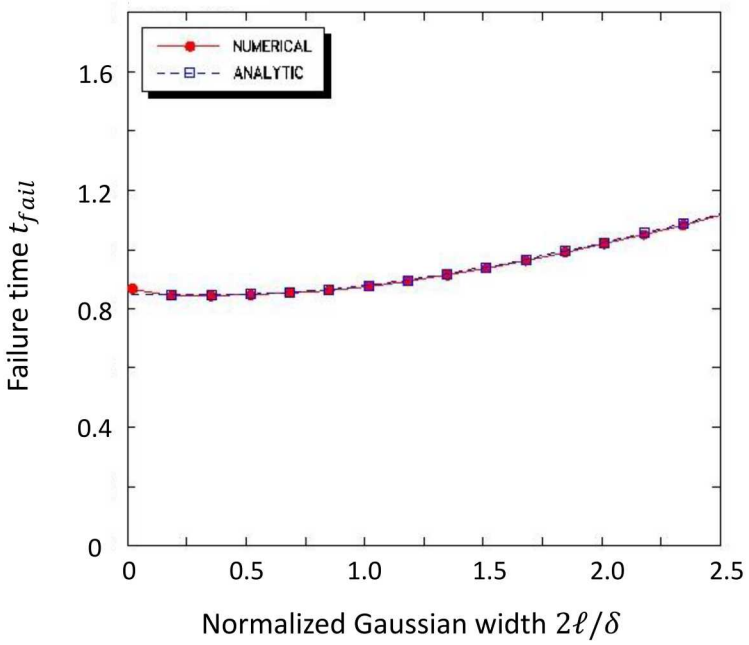

Figure 8. Failure times for an initial Gaussian perturbation $\tilde{u}$ superposed on a homogeneous strain in the descending part of the material model. The solid blue line is from the direct numerical simulation; the red dashed line is from the analytical expression (59).

Figure 8 shows a graph of the failure time t_{fail} as a function of the half-width ℓ of the Gaussian function in the initial perturbation. The material model parameters are $\delta = 0.1$, $E = 1$, $\rho = 1$, $s_1 = 0.05$, $s_0 = 0.20$. The peak strain in the initial perturbation 1.0×10^{-6}. The failure times found by solving the equation (59) and by direct numerical simulation are shown, which agree closely.

8 Stretching of a bar with a defect

Consider an infinite bar composed of the material (26), but with a small heterogeneity:

$$F(\eta,\xi,x) = h\left(x+\frac{\xi}{2}\right)\frac{\xi}{\delta}\begin{cases} cs & \text{if } s < s_1, \\ cs_1(s_0-s)/(s_0-s_1) & \text{if } s_1 \le s < s_0, \\ 0 & \text{if } s_0 \le s \end{cases} \tag{62}$$

$\forall x,\ \forall\eta\ \forall\xi$ where h is a function defined by

$$h(z) = 1 - h_0 e^{-(z/\ell)^2} \qquad \forall z \tag{63}$$

in which h_0 and ℓ are positive constants, $h_0 \ll 1$. In effect, this material description adds a soft spot near $x = 0$.

Now suppose the bar is subjected to a zero displacement, constant strain rate initial condition:

$$u(x,0) = 0, \qquad \dot{u}(x,0) = r_0 x \qquad \forall x \tag{64}$$

where r_0 is the initial strain rate. We now investigate the failure time, at which the local strain at $x = 0$ first exceeds s_0. Since h_0 is small, wave propagation prior to when the peak in the material model is reached will be neglected. The soft spot in the bar results in a small variation in local strain and strain rate. Therefore, at the time $t_p = s_1/r_0$ when the peak s_1 in the material model is reached,

$$\tilde{u}_x(x,t_p) = s_1 h_0 e^{-(x/\ell)^2}, \quad \dot{\tilde{u}}_x(x,t_p) = r_0 h_0 e^{-(x/\ell)^2} \qquad \forall x. \tag{65}$$

The expressions (65) in effect supply initial conditions for when the bar enters the downward sloping segment of the material model. Setting $\epsilon_0 = s_1$, this is essentially the same problem as was studied in Section 7, but with an initial perturbation in strain rate as well as strain. Repeating the analysis of Section 7, after modifying it to include nonzero initial strain rates, (56) now becomes

$$\tilde{u}_x(0,t) = \frac{\ell h_0}{2\sqrt{\pi}}\int_{-\infty}^{\infty} e^{-(\ell k/2)^2}\Big[s_1\cosh(\lambda(k)(t-t_p)) + \frac{r_0}{\lambda(k)}\sinh(\lambda(k)(t-t_p))\Big]\,dk, \qquad t > t_p. \tag{66}$$

At the time of failure,

$$s_0 - s_1 = r_0(t_{fail}-t_p) + \frac{\ell h_0}{2\sqrt{\pi}}\int_{-\infty}^{\infty} e^{-(\ell k/2)^2}\Big[s_1\cosh(\lambda(k)(t_{fail}-t_p)) + \frac{r_0}{\lambda(k)}\sinh(\lambda(k)(t_{fail}-t_p))\Big]\,dk. \tag{67}$$

Now assume that r_0 and ℓ are both small. The following approximation to (67) therefore applies:

$$s_0 - s_1 \approx \frac{\ell h_0}{2\sqrt{\pi}}\left(\int_{-\infty}^{\infty} e^{-(\ell k/2)^2}\,dk\right)\left(\frac{s_1}{2}+\frac{r_0}{2\lambda_\infty}\right)e^{\lambda_\infty(t_{fail}-t_p)} \tag{68}$$

where λ_∞ is defined in (57). Solving (68) for t_{fail} leads to

$$t_{fail} \approx \min\left\{\frac{s_0}{r_0}, \left[\frac{s_1}{r_0}+\frac{1}{\lambda_\infty}\log\left(\frac{2(s_0-s_1)}{h_0(s_1+r_0/\lambda_\infty)}\right)\right]\right\} \tag{69}$$

where the minimum appears because s_0/r_0 is the time it would take to fail the material if no exponential growth at the weak spot occurred.

Figure 9 shows the failure time for the material in (26) for a range of strain rates r_0, a weak spot of half-width $\ell = 2\delta$ and amplitude $h_0 = 0.01$. The material model parameters are $\delta = 0.1$, $E = 1$, $\rho = 1$, $s_1 = 0.05$, $s_0 = 0.20$. The figure compares the numerical results with the approximate failure time in (69). The straight lines correspond to the minimum and maximum possible failure times of s_1/r_0 and s_0/r_0. The results show that slow loading (low r_0) causes the material to fail a short time after it passes the peak in the curve of bond force vs. bond strain at s_1. During this time, the instability causes the pulse to grow until its maximum strain exceeds s_0, which is our definition of failure.

For the same problem, Figure 10 shows, on the left, how the failure time depends on h_0, with horizon $\delta = 0.1$, bulk strain rate $r_0 = 0.05$, and defect half-width $\ell = 2\delta$. On the right is a graph of failure time as the defect half-width ℓ is varied, with horizon $\delta = 0.1$, bulk strain rate $r_0 = 0.05$, and $h_0 = 0.01$. Both these dependencies are weaker than the dependence on bulk strain rate, which is shown in Figure 9.

At higher strain rates, the unstable growth is more rapid, because the strain rate at the weak spot contributes to the initial perturbation as the strain passes the peak. This is seen in the sinh term in (66). At very high strain rates, even with the contribution of this perturbation in strain rate, there is not enough time for the instability to grow significantly before the bulk strain $r_0 t$ exceeds s_0. In this case, the failure time given approximately the same as the "maximum" line in Figure 9.

The evolution of the displacement field is shown for six different times Figure 11. After the failure time, a crack appears at $x = 0$. Because this crack unloads the material, compressive release waves propagate away from the crack. All the curves in this figure come from a direct numerical simulation with $\delta = 0.1$, $\ell = 2\delta$, $r_0 = 0.05$, and $h_0 = 0.01$. For the same simulation, Figure 12 shows the nonlocal stress $\sigma(0, t)$ defined by

$$\sigma(x,t) = \int_0^\delta \int_z^\delta f(x - z + \xi, x - z, t)\, d\xi\, dz \qquad \forall x,\ \forall t \tag{70}$$

where f is the pairwise bond force density. (Equation (27) is a special case of (70) for constant strain.)

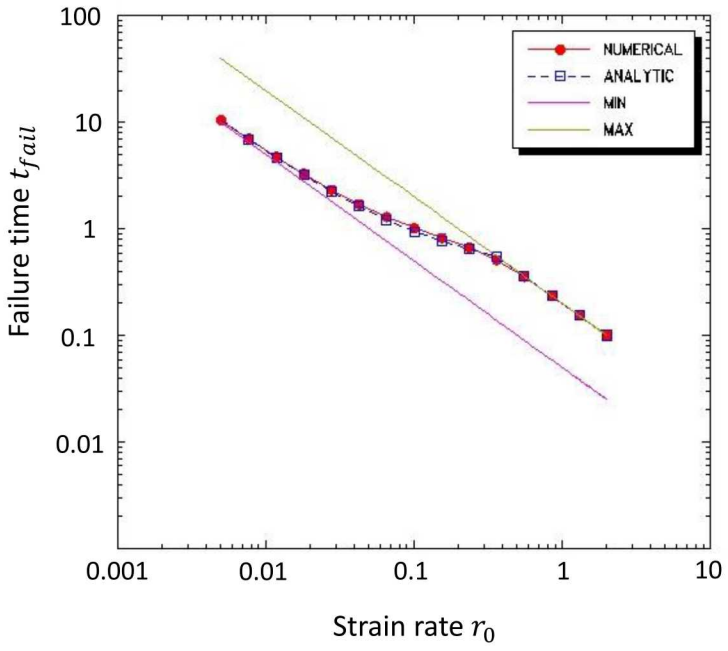

Figure 9. Failure times for the stretching of a bar with a soft spot. The solid blue line is from the direct numerical simulation; the red dashed line is from the analytical expression (69).

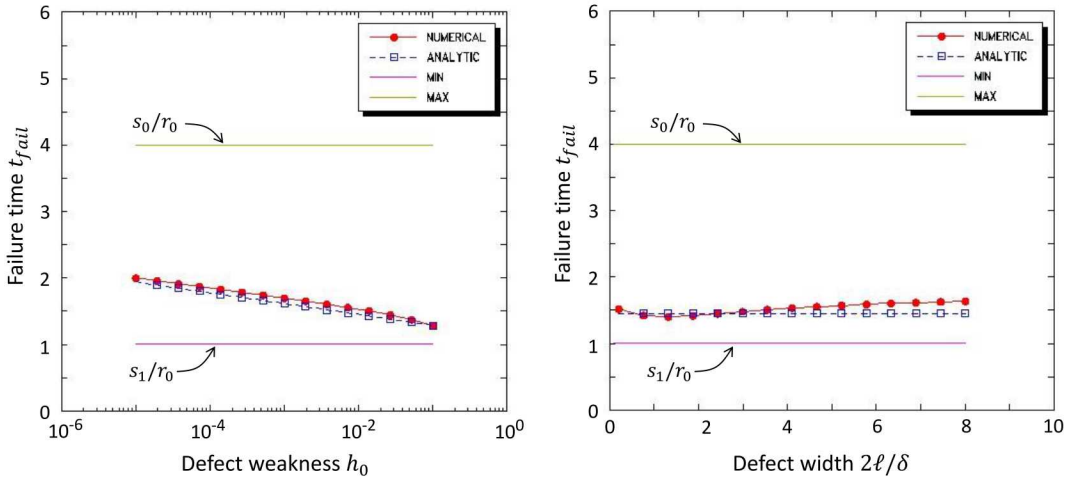

Figure 10. Failure times for the stretching of a bar with a soft spot. The solid blue line is from the direct numerical simulation; the red dashed line is from the analytical expression (69). Left: dependence on the initial defect weakness h_0. Right: dependence on the defect half-width ℓ.

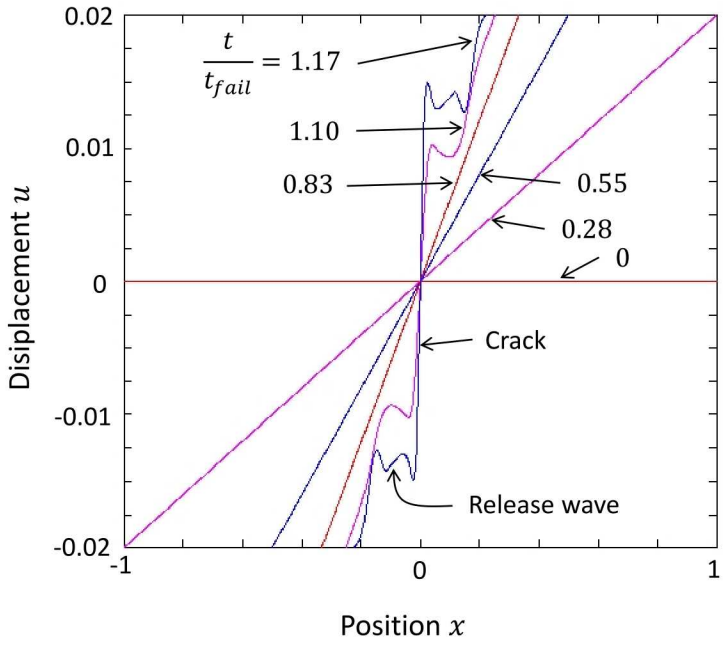

Figure 11. Pre- and post-failure behavior of a bar with a soft spot under tension. A crack and release waves rapidly appear after the failure time is reached.

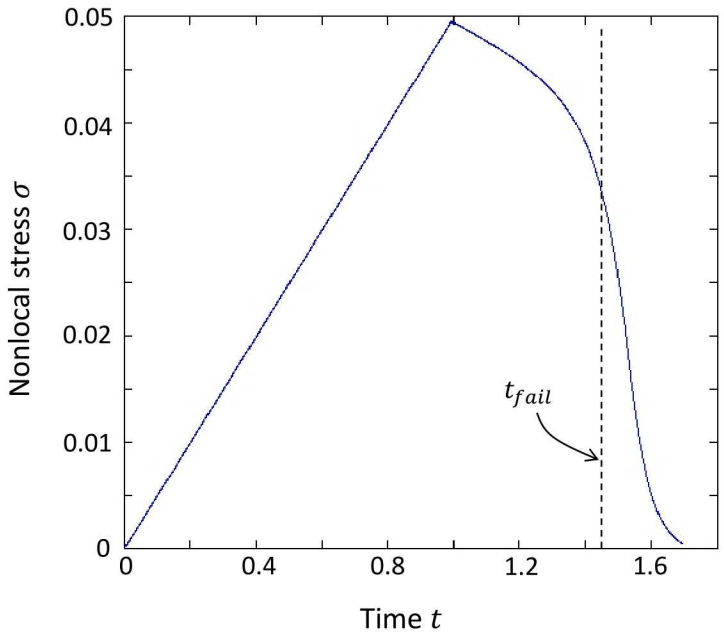

Figure 12. Nonlocal stress as a function of time at the center of the defect as the bar is stretched.

9 Rate effect

The results of the previous section for the failure time in a stretching bar with a defect can be interpreted as a rate effect. Define the *bulk failure strain* ϵ_{fail} to be the bulk strain (at points far from the weak spot) when the bar fails:

$$\epsilon_{fail} = r_0 t_{fail}. \tag{71}$$

From (69) and (71),

$$\epsilon_{fail} \approx \min\left\{s_0, \left[s_1 + \frac{r_0}{\lambda_\infty}\log\left(\frac{2(s_0 - s_1)}{h_0(s_1 + r_0/\lambda_\infty)}\right)\right]\right\}. \tag{72}$$

An interesting observation from (72) is that the strain rate appears only in the dimensionless term r_0/λ_∞, that is, only in proportion to the blow-up rate for the material. Since (61) continues to hold,

$$\frac{r_0}{\lambda_\infty} = \frac{r_0\delta}{\mathcal{C}}\sqrt{\frac{s_0 - s_1}{6s_1}}. \tag{73}$$

Figure 13 shows analytical and numerical results for the bulk failure strain as a function of bulk strain rate for the same problem as in the previous section, the stretching of a bar with a defect. At low strain rates ($r_0/\lambda_\infty \ll 1$), the rate effect is small, and $\epsilon_{fail} \approx s_1$. At intermediate strain rates, it becomes larger. At high strain rates, the rate effect saturates and the failure strain follows $\epsilon_{fail} \approx s_0$. Both these limiting behaviors at slow and large strain rates are reasonable physically.

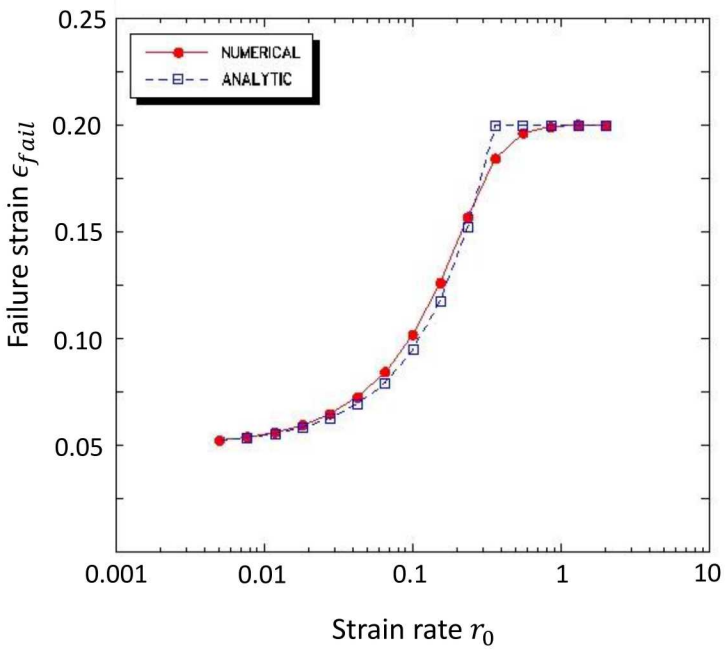

Figure 13. Bulk failure strain for the stretching of a bar with a soft spot plotted as a function of strain rate. The solid blue line is from the direct numerical simulation; the red dashed line is from the analytical expression (72).

10 Discussion

Rate dependence of failure in many kinds of materials can be attributed to microstructural events such as the growth and interaction of microcracks that are too small or too fast to be incorporated explicitly in a macroscopic engineering simulation. In this sense, incorporation of rate dependence in a typical material model is a type of multiscale or upscaling method. However, careful analysis at small length scales can predict failure times, or incubation times, of an assumed initial microstructure under loading [21]. These failure times can be interpreted as rate effects.

The results in the present paper show that failure times and the resulting rate effects can be reproduced in a peridynamic material model that includes an unstable branch but no explicitly rate-dependent terms. As demonstrated in Figures 9 and 10, the predicted dependences on the weakness and length scale of a small defect are much less significant than the dependence on the strain rate.

The conclusion is that for some materials and applications, a suitable nonconvex peridynamic elastic model can be used in a numerical simulation to treat, implicitly, an incubation time for material failure without computing or incorporating this incubation time explicitly. Thus, such a peridynamic model can be interpreted as a kind of coarse graining approach to the modeling of microstructural processes that culminate in material failure.

The most commonly used peridynamic material models for brittle materials assume an increasing bond force vs. bond strain curve up to the point of bond breakage. An example of such a model is the microelastic brittle material described in [25]. Sudden bond breakage can be viewed as a limiting case of the nonconvex material model (26) with $s_0 \to s_1$. In this limit, (57) implies that $\lambda_\infty \to \infty$, so the rate effect vanishes. This suggests that a rate effect could be added to a simple bond breakage material model by adding a tail to the bond force curve, that is, setting s_0 large enough to achieve the desired effect. This approach could be an alternative to adding terms to the simple model that explicitly include a rate dependence in the critical bond strain for breakage.

The stretching bar problem considered in Section 8 demonstrates the nucleation of a crack. However, it can be thought of as a one-dimensional model problem for a growing crack. If, instead of a bar, one considers a cross-section of a two-dimensional body that is transverse to a growing crack (Figure 14), the strain concentration near the crack tip supplies a perturbation similar to the initial data in the one-dimensional problem. If the process zone of the crack contains unstable material, the one-dimensional cross-section will eventually become unstable as well, setting off the chain of events described in Section 8 leading to the appearance of a discontinuity. Viewed in this way, the results of this paper may offer insight into the difficult question of what really happens as a crack grows: how does a material point where the deformation is smooth transform into a point of discontinuity?

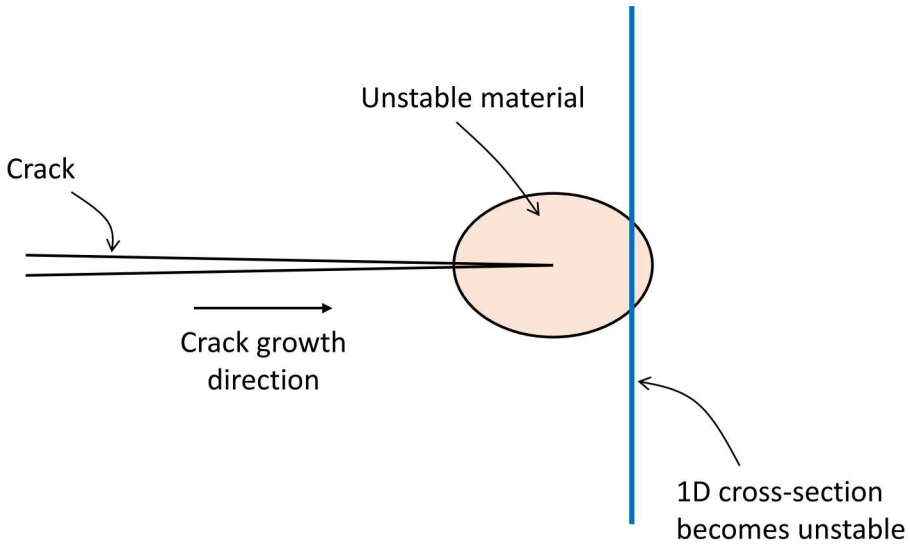

Figure 14. Cross-section in front of an advancing crack enters a region of material instability as it becomes consumed by the process zone.

References

[1] A. R. Aguiar, G. F. Royer-Carfagni, and A. B. Seitenfuss. Wiggly strain localizations in peridynamic bars with non-convex potential. *International Journal of Solids and Structures*, 138:1–12, 2018.

[2] T. Belytschko and J.-H. Song. Coarse-graining of multiscale crack propagation. *International journal for numerical methods in engineering*, 81:537–563, 2010.

[3] V. Bratov and Y. Petrov. Application of incubation time approach to simulate dynamic crack propagation. *International Journal of Fracture*, 146:53–60, 2007.

[4] K. Dayal and K. Bhattacharya. Kinetics of phase transformations in the peridynamic formulation of continuum mechanics. *Journal of the Mechanics and Physics of Solids*, 54:1811–1842, 2006.

[5] J. L. Ericksen. Equilibrium of bars. *Journal of Elasticity*, 5(3):191–201, 1975.

[6] R. D. James. Co-existent phases in the one-dimensional static theory of elastic bars. *Archive for Rational Mechanics and Analysis*, 72:99–140, 1979.

[7] P. K. Jha and R. Lipton. Finite element approximation of nonlinear nonlocal models. *arXiv preprint arXiv:1710.07661*, 2017.

[8] P. K. Jha and R. Lipton. Finite difference approximation for state based peridynamic fracture models. *arXiv preprint arXiv:1805.00296*, 2018.

[9] P. K. Jha and R. Lipton. Numerical analysis of nonlocal fracture models in holder space. *SIAM Journal on Numerical Analysis*, 56:906–941, 2018.

[10] J. K. Knowles and E. Sternberg. On the ellipticity of the equations of nonlinear elastostatics for a special material. *Journal of Elasticity*, 5:341–361, 1975.

[11] J. K. Knowles and E. Sternberg. On the failure of ellipticity of the equations for finite elastostatic plane strain. *Archive for Rational Mechanics and Analysis*, 63(4):321–336, 1976.

[12] J. K. Knowles and E. Sternberg. On the failure of ellipticity and the emergence of discontinuous deformation gradients in plane finite elastostatics. *Journal of Elasticity*, 8:329–379, 1978.

[13] A. Kobayashi, M. Ramulu, M. Dadkhah, K.-H. Yang, and B. Kang. Dynamic fracture toughness. *International Journal of Fracture*, 30:275–285, 1986.

[14] I. A. Kunin. *Elastic Media with Microstructure I: One-Dimensional Models*. Springer: Berlin, 1982.

[15] R. Lipton. Dynamic brittle fracture as a small horizon limit of peridynamics. *Journal of Elasticity*, 117:21–50, 2014.

[16] R. Lipton. Cohesive dynamics and brittle fracture. *Journal of Elasticity*, pages 1–49, 2015.

[17] R. Lipton, R. Lehoucq, and P. Jha. Complex fracture nucleation and evolution with nonlocal elastodynamics. *Journal of Peridynamics and Nonlocal Modeling*.

[18] R. Lipton, E. Said, and P. Jha. Free damage propagation with memory. *Journal of Elasticity*, 133:129–153, 2018.

[19] R. Lipton, E. Said, and P. K. Jha. Dynamic brittle fracture from nonlocal double-well potentials: A state-based model. *Handbook of Nonlocal Continuum Mechanics for Materials and Structures*, pages 1–27, 2018.

[20] T. Mengesha and Q. Du. Analysis of a scalar peridynamic model with a sign changing kernel. *Discrete Contin. Dynam. Systems B*, 18:1415–1437, 2013.

[21] S. Nemat-Nasser and H. Deng. Strain-rate effect on brittle failure in compression. *Acta Metallurgica et Materialia*, 42:1013–1024, 1994.

[22] Y. V. Petrov. Incubation time criterion and the pulsed strength of continua: fracture, cavitation, and electrical breakdown. *Doklady Physics*, 49:246–249, 2004.

[23] S. Silling, O. Weckner, E. Askari, and F. Bobaru. Crack nucleation in a peridynamic solid. *International Journal of Fracture*, 162(1-2):219–227, 2010.

[24] S. A. Silling. Reformulation of elasticity theory for discontinuities and long-range forces. *Journal of the Mechanics and Physics of Solids*, 48:175–209, 2000.

[25] S. A. Silling and E. Askari. A meshfree method based on the peridynamic model of solid mechanics. *Computers and Structures*, 83:1526–1535, 2005.

[26] S. A. Silling and R. B. Lehoucq. The peridynamic theory of solid mechanics. *Advances in Applied Mechanics*, 44:73–166, 2010.

[27] L. Truskinovsky and G. Zanzotto. Finite-scale microstructures and metastability in one-dimensional elasticity. *Meccanica*, 30(5):577–589, 1995.

DISTRIBUTION:

1	MS 0899	Technical Library, 9536 (electronic copy)
1	MS 0359	D. Chavez, LDRD Office, 1911

Sandia National Laboratories